Journal of Materials Chemistry A

Accepted Manuscript

ROYAL SOCIETY OF CHEMISTRY

www.rsc.org/materialsA

Hierarchical Three-Dimensional Mesoporous MnO_2 Nanostructure for High Performance Aqueous Asymmetric Supercapacitor

*Sourav Bag and C. Retna Raj**

Functional Materials and Electrochemistry Laboratory, Department of Chemistry,
Indian Institute of Technology Kharagpur, Kharagpur 721302, India.
Fax: +91 3222-282252;
Tel: +91 3222-283348
E-mail: crraj@chem.iitkgp.ernet.in

Abstract

We describe a new facile chemical route for the synthesis of hierarchical mesoporous α-MnO_2 and the development of aqueous asymmetric supercapacitor. The hierarchical α-MnO_2 is synthesized by the thermodynamically favorable redox reaction between metallic Zn and MnO_4^- in mild acidic solution without any template. Zn and the in situ generated nascent hydrogen efficiently reduce MnO_4^- to MnO_2. The growth mechanism is studied with time-dependent electron microscopic measurements. The α-MnO_2 has three-dimensional (3D) flower-like mesoporous hierarchical structure with an average size of 500 nm and large surface area (206 m^2g^{-1}) with a pore size of 48.34 Å and pore volume of 0.543 cc g^{-1}. It has significantly high electronic conductivity with respect to traditional/commercial MnO_2. Specific capacitance as high as 322 F g^{-1} at a current density of 1 A g^{-1} with excellent cycling stability (90% after 8000 cycles) is achieved. Aqueous asymmetric supercapacitor (ASC) is developed by pairing α-MnO_2 and reduced graphene oxide-based electrodes. ASC could deliver a specific capacitance of 63.5 F g^{-1} at 2 A g^{-1} with a potential window of 0-2 V. ASC retains 100% initial specific capacitance even after 3000 continuous charge-discharge cycles. It has the energy density of 35.28 Wh kg^{-1} at the power density of 2.0 kW kg^{-1} and could retain 27.78 Wh kg^{-1} at a power density of 16.67 kW kg^{-1}. The three-dimensional mesoporous structure favors the facilitated transport of electrolyte across the electrode. The post-mortem XRD analysis shows that the MnO_2 nanostructures retain its initial α phase even after 3000 charge-discharge cycles, though a partial disintegration of the hierarchical structure was observed.

Keywords: mesoporous manganese dioxide, three-dimensional, asymmetric supercapacitor, energy storage

1. Introduction

Development of energy storage devices of high energy density and long life cycle is one of the pressing needs of the automotive and electronic industries. The renewable energy sources (solar, wind, etc.) of low emission are limited by time and an ideal energy storage system is critically required to assure a balanced power supply. Batteries and supercapacitors are very promising for the storage of energy generated from the renewable sources. In the recent years, supercapacitors, the complementary energy storage device to battery, received significant attention though they have low energy density compared to batteries.[1] The ultrahigh power density, fast charge-discharge, long life cycle and safety are the fascinating features of supercapacitors.[2,3] They can be conveniently coupled with the energy conversion device such as fuel cell to serve as an efficient energy storage system for continued power supply.[4] They can also serve as a stand-alone energy supply system for many applications.[1] Based on the charge storage mechanism, the supercapacitors can be classified into two categories: (i) electrical double layer supercapacitors and (ii) pseudocapacitors. In the former case, the charge storage mechanism involves the adsorption of electrolyte ion at the electrode-solution interface. On the other hand, in the case of pseudocapacitors, the energy storage involves the charge transfer at the electrode-solution interface.

The energy density of supercapacitor mainly depends on the nature of electrode materials. Several attempts have been made in the past to develop materials that are capable of delivering high energy density.[1] Carbon, transition metal oxides and conducting polymer-based materials have been traditionally used. The use of conductive ordered/disorderd mesoporous material of large surface area is a promising approach to enhance the energy density of supercapacitors.[5-8] It has been demonstrated that the ordered mesoporous carbon based materials have superior capacitive performance.[5-10] Facilitated electron and ion transport, high electronic conductivity, large surface area, etc. are the primary requirements

of the electrode material for high energy supercapacitors.[11-13] Among the transition metal oxides, MnO_2-based materials are very attractive as they are cost-effective, environment friendly and they can be synthesized in large scale.[14] Although MnO_2 has excellent theoretical capacitance of 1370 F g^{-1}, the poor electronic conductivity of MnO_2 limits the facilitated ion/electron transport and hence a poor capacitive performance.[14] Various strategies have been used to improve the capacitive performances of MnO_2.[15-24] The conductive carbon has been widely used along with MnO_2 to enhance the capacitive performance. For instance, MnO_2 nanowires deposited onto carbon nanotube (CNT) could deliver a specific capacitance of 167.5 F g^{-1} at the current density of 77 mA g^{-1}.[25] Very recently, Li et al. reported the supercapacitive performance of CNT-MnO_2 composite electrode with the specific capacitance of 201 F g^{-1} at 1 A g^{-1} and excellent cycling stability.[26] The CNT-MnO_2 based supercapacitor electrodes could deliver the specific capacitance ranging from 100-300 F g^{-1}, depending on the current density/sweep rate.[26-28] In the recent years, nanostructured MnO_2 based composite material with graphene/reduced graphene oxide (rGO) and rGO/CNT-MnO_2 composite electrodes have also been studied for supercapacitor applications.[29-32] It is generally accepted that the materials which favors facilitated ion/electron transport and have high electronic conductivity and minimum diffusion length would deliver high specific capacitance. Facilitated ion transport and short diffusion length can be achieved with the materials of very small size and conductive hierarchical mesoporous 3D nanostructures. The mesoporous structures can significantly decrease the ion transport limitations and enhance the supercapacitive performance. Traditionally, the porous hierarchical nanostructures have been synthesized using templates such as surfactants and by controlling the growth kinetics. Only handful of reports describe the synthesis of mesoporous MnO_2 without any template.[33-37] The hydrothermal procedures have been often employed to obtain mesoporous MnO_2 nanostructures.[33,35] Herein, for the first time, we describe a novel

non-hydrothermal and template-free route for the synthesis of 3D hierarchical mesoporous α-MnO_2 and the development of aqueous asymmetric supercapacitor with excellent performance. Our method is simple, novel and we could obtain the hierarchical nanostructure in 2 h time. The performance of the ASC is evaluated in terms of specific capacitance, energy density, rate capability and recyclability.

2. EXPERIMENTAL SECTION

2.1 Materials and methods

Graphite, zinc powder, N-methyl-2-pyrrolidone (NMP) and polyvinylidene fluoride (PVF) were obtained from Sigma-Aldrich. All the other chemicals used in this investigation were of analytical grade and obtained from Merck, India. All the solutions were prepared with Millipore water (Milli-Q system).

2.2 Synthesis of mesoporous α-MnO_2

In a typical procedure, 20 mg of $KMnO_4$ was dissolved in 20 mL of 0.1 M H_2SO_4 solution. Required amount of Zn powder was added to the solution and stirred at room temperature for 2 h or until the metallic Zn is consumed completely. The thus obtained black colored mesoporous α-MnO_2 was washed repeatedly with copious amount of water and alcohol to remove the unreacted $KMnO_4$ and Zn. MnO_2 samples containing different atomic % of Zn/Zn(II) was obtain by controlling the initial amount of metallic Zn in the reaction vessel.

2.3 Synthesis of rGO

Graphene oxide (GO) was prepared by the exfoliation of graphite using modified Hummers' method.[12,38] GO was reduced to rGO by refluxing with ethylene glycol at 180^{o}C for 3 h. The black colored rGO was washed extensively with water and dried in vacum for an hour.

2.4 Electrode preparation

The working electrode was prepared by mixing mesoporous α-MnO_2 (80%) with acetylene black (15%) and PVF (5%) dissolved in NMP in a mortar pestle. The obtained slurry was then uniformly coated on a nickel foil current collector and dried in a vacuum oven at 60 °C for 12 h. The loading of mesoporous α-MnO_2 onto the current collector was optimized and high specific capacitance was obtained at a loading of 1 mg cm^{-2}. The rGO based electrode was prepared by mixing with PVF binder in 9:1 weight ratio in NMP solvent. All electrochemical experiments were performed under an inert atmosphere and Na_2SO_4 (1 M) was used as an electrolyte. The ASC was developed by pairing the α-MnO_2 with rGO-based anode. Circular wafers (diameter: 1.0 cm, thickness: 200 μm) of the electrode material was obtained by pressing at a pressure of 5 kPa. The mass of α-MnO_2 in the circular wafer was 0.8 mg (~1 mg/cm^2). The mass ratio of the two electrode material in ASC was calculated from the charge balance of the two electrodes, following our previous method (ESI).[12] A separator soaked in 1 M Na_2SO_4 was placed between the two electrodes and then it was placed into a stainless steel split flat cell for the capacitance measurements. For post-mortem analysis of the electrode material, mesoporous α-MnO_2 was mixed with PVF binder in a ratio of 9:1 in NMP solvent and coated over the Ni foil. Acetylene black was not added for better understanding of the changes in the morphology. The electrode material on the current collector was subjected to 3000 charge-discharge cycles and then used in the post-mortem analysis.

2.5 Capacitance measurement

The specific capacitance of the three- and two-electrode system was calculated from the charge-discharge profile using the following equation:[2,39,40]

$$C_s = \frac{i_d \times \Delta t_d}{\Delta V} \ldots \ldots \ldots (1)$$

where C_s is the specific capacitance of the electrode material or the supercapacitor device; i_d is the applied constant current density during charge and discharge; Δt_d is the time taken for complete discharge and ΔV is the potential window for discharge. Coulombic efficiency of the electrode was calculated from the following equation (2)[41]

$$\eta = \frac{\Delta t_d}{\Delta t_c} \times 100 \ldots\ldots\ldots (2)$$

where Δt_c is the time taken for complete charge. Energy density (E) and power density (P) was calculated using equations (3) and (4)[2,39,40]

$$E = \frac{1}{2} \times C_s \times \Delta V^2 \ldots\ldots\ldots (3)$$

$$P = \frac{E}{\Delta t_d} \ldots\ldots\ldots (4)$$

2.6 Characterization

Transmission electron microscopic (TEM) measurements were performed with FEI-TECNAI G2 20S TWIN electron microscope operating at a voltage of 200 kV. Carbon coated copper grid was used for sample preparation. Field emission scanning electron microscopic (FESEM) analysis was performed using FEI NOVA NANOSEM 450, and mapping analysis was carried out with BRUKER EDS microanalyzer attached to the FESEM instrument. XRD profiles were acquired with BRUKER D8 advance unit using Cu-Kα (λ = 1.54 Å) radiation. The X-ray photoelectron spectroscopic (XPS) measurements were carried out with PHI 5000 Versaprobe II scanning XPS microscope using Al as the energy source (Kα, hν = 1486.6 eV). Raman spectroscopic measurements were taken using a Jobin Yvon Horiba T64000 spectrometer (France) with an excitation source of Argon Krypton mixed ion gas laser (488 nm, Spectra Physics, USA). For conductivity measurement, α-MnO_2 powder sample was dispersed in NMP (1 mg mL^{-1}) and sonicated for 1 h. After sonication, a uniform ink was formed and it coated over a glass slide. The film on the glass slide was dried in a

vacuum oven for overnight. The conductivity measurement of the film was performed with Vander Pauw 4 probe electrical measurement technique using ECOPIA HMS -3000 Hall measurement unit. All the electrochemical experiments were performed with Autolab potentiostat/galvanostat (302N) with computer controlled NOVA software in a single compartment three-electrode electrochemical cell with Ag/AgCl (3 M KCl) as a reference and Pt foil as counter electrodes. The stainless steel split flat cell (MTI Corporation) was used in the capacitance measurement of ASC.

3. RESULTS AND DISCUSSION

3.1 Synthesis and material characterization

Our synthetic method involves the thermodynamically favourable Zn-mediated reduction of $KMnO_4$ in aqueous acidic solution at room temperature (Scheme 1). The reduction potential of Zn(II)/Zn (-0.76 V) and MnO_4^-/MnO_2 (1.76 V) redox couples suggest that MnO_4^- can be conveniently reduced to MnO_2 by metallic Zn under optimized conditions. Zn metal can undergo two parallel reactions in aqueous acidic solution containing MnO_4^- ions: (i) facile reduction of MnO_4^- to low valent Mn species including MnO_2 and (ii) reduction of proton and the evolution of nascent hydrogen. It is worth pointing out here that although the E^0 of H^+/H_2 is lower than that of MnO_4^-/MnO_2, simultaneous reduction of MnO_4^- as well as H^+ was observed (both reactions have negative ΔG). The in situ generated nascent hydrogen is capable of efficiently reducing MnO_4^- to MnO_2. In the presence of optimized amount of Zn and H^+ ions, MnO_4^- has been quantitatively reduced to MnO_2. Evolution of nascent hydrogen was clearly seen with the naked eye in the reaction vessel. The evolution of nascent hydrogen and the dissolution of Zn favor the growth of porous MnO_2 nanostructure as shown in Scheme 1. Our method is simple and superior to that of the existing method[42] as it does not require any templates or surfactants and the growth of MnO_2 was achieved at room temperature in 2 h time (Table S1).

The electron microscopic images show the growth of hierarchical 3D flower-like MnO_2 structures with an average size of 500 nm (Figure 1). It is obvious from the magnified image that the hierarchical structure is actually made of the assembly of crumbled nanosheets of thickness ~5 nm. The nanosheets are crumpled and disorderly interconnected, making the material highly porous. The high resolution TEM image shows fringe spacing of 4.9, 3.5, 3 and 2.5 Å, corresponding to the (200), (220), (310) and (400) planes, respectively, of α-MnO_2 (ESI 1). The growth mechanism was investigated by time-dependent electron microscopic measurements at different time interval of the reaction. The reaction between Zn and MnO_4^- is very fast in acidic solution and it is rather difficult to separate the product from the reaction mixture at the initial stage (<15 min) of the reaction. Brownish black color was noticed immediately after the addition of Zn into the reaction mixture, suggesting the instant reduction of MnO_4^- to MnO_2. To understand the growth mechanism the product of the reaction was collected at different time intervals (~15 and 60 min) and the corresponding TEM and FESEM images are shown in Figure 2 and ESI 2. As can be seen that the α-MnO_2 nanostructures obtained at 15 min of the reaction have hierarchical morphology with size ranging from 150-300 nm (Figure 2a-c), which is much smaller than the final product obtained after the 2 h of the reaction (500 nm). The TEM image and the EDS profile obtained at 15 min shows the presence of unreacted Zn (Figure 2a-c and ESI 3). On the other hand, the α-MnO_2 nanostructures obtained at 60 min of the reaction are larger in size (~400 nm). No signature for the presence of Zn was obtained after 60 min of the reaction, suggesting that the Zn metal is consumed during the reaction. Both the Zn and the in situ generated nascent hydrogen effectively reduce MnO_4^- to MnO_2. With time the MnO_2 nanostructure further grow and attained the size of ~500 nm at the completion of the reaction (2 h). No further change in the size and surface morphology was noticed after 2 h of the reaction. The reaction requires minimum amount of acid and it does not proceed in the absence of acid.

The X-ray diffraction profile (Figure 3) shows characteristic diffraction for the (200), (310), (211), (521) and (002) planes of α-MnO_2 (JCPDS file no 44-0141). All these diffractions are in excellent agreement with the electron microscopic measurements (ESI 1). The XPS profile of MnO_2 shows signature for the elements C, O, Mn and Zn (Figure 4). The Mn 2p signal appear at the binding energy of 653.7 ($2p_{3/2}$) and 642.1 ($2p_{1/2}$) eV with an energy separation of 11.78 eV, which is in accordance with the literature.[15-17,43] On the other hand, the Mn 3s signal appears at the binding energy of 88.32 and 83.51 eV with an energy separation of 4.81 eV (Figure 4).[15,43] The XPS signal for Zn is due to the presence of trace amount of Zn used in the reaction (vide supra). The α-MnO_2 is known to exhibit two diagnostic Raman spectral bands in the high frequency region corresponding to the A_g mode. In our case, the Raman spectral profile (ESI 4) shows an intense peak ~ 650 cm^{-1} due to symmetric stretching vibration of the MnO_6 octahedra (Mn-O bond).[44,45] The peak appears at 575 cm^{-1} corresponds to the stretching vibration of the basal plane of MnO_2.[46] It should be mentioned here that MnO_2-based material is known to undergo laser-induced structural changes during the Raman measurement due to local heating.[46] The other weak bands observed could be due to the structural changes during the measurement.

The surface area and porosity of the material was examined with adsorption-desorption experiments using Brunauer-Emmett-Teller (BET) method (Figure 5). The adsorption-desorption profile indicates that α-MnO_2 has type IV isotherm, suggesting the mesoporous nature of the material. The pore size analysis performed using Barrett−Joyner−Halenda method shows that α-MnO_2 has very narrow pore size with an average pore diameter of 48.34 Å. The average pore volume was estimated to be 0.543 cc g^{-1}. It has very large specific surface area of 206 m^2/g, which is significantly higher than the commercial MnO_2[47] and MnO_2 nanostructure reported in the literature[42,48] (Table S1). As our α-MnO_2 is mesoporous and have very large specific surface area it is very promising for

supercapacitor application.

The commercial/traditional MnO_2 has very poor electrical conductivity (10^{-6} to 10^{-5} S/cm) and it significantly limits the power performance and rate capability, though MnO_2 has very high theoretical specific capacitance.[14,49] Our as-synthesized hierarchical mesoporous α-MnO_2 in the absence of any additive has the conductivity of 7.29×10^{-4} S cm^{-1}, which is significantly higher than the commercial MnO_2. Such high conductivity assures enhanced supercapacitive performance. The high electrical conductivity may be ascribed to the presence of trace amount of Zn or Zn(II) ions in the tunnels. The crystal structure of α-MnO_2 has [1x1] and [2x2] tunnels (Scheme 2) along the c-axis of the tetragonal unit cell.[48] Both the [1x1] and [2x2] tunnels can accommodate Zn or Zn(II). The reversible intercalation of Zn(II) into the tunnels of α-MnO_2 is well known in the chemistry of rechargeable Zn ion battery.[50-52] The amount of Zn/Zn(II) was quantified from the XPS and EDS measurements and was very less with respect to the other elements (ESI 5). The atomic % of Zn/Zn(II) was obtained from the EDS and XPS profiles and was 0.98% (ESI 5 and Figure 4). In the XPS profile, the Zn $2p_{1/2}$ and $2p_{3/2}$ peaks appear at the binding energy of 1041 and 1021 eV, respectively, further confirming the presence of Zn. In order to further understand the effect of Zn/Zn(II) content in the conductivity, three different α-MnO_2 samples with varying atomic % of Zn/Zn(II) have been synthesized. It was observed that the amount of Zn/Zn(II) significantly influences the conductivity of the samples. An increase in the conductivity while increasing the atomic % Zn was noticed (Table S2).

3.2 Electrochemical studies

The supercapacitive performance of mesoporous α-MnO_2 was examined with cyclic voltammetric, charge-discharge and electrochemical impedance measurement in three and two-electrode configurations in 1 M Na_2SO_4. The as-synthesized mesoporous α-MnO_2 was mixed with acetylene black and PVF to prepare the electrode. Nickel foil was used as the

conducting substrate to support the electrode material in the three-electrode electrochemical studies. Figure 6a represents the typical voltammetric response of mesoporous α-MnO_2 with the three-electrode configuration. Rectangular shape voltammetric response with a potential window of 0-1 V was obtained, indicating the capacitive behaviour of the electrode material. The charge storage in the MnO_2-based materials is associated either with the intercalation/de-intercalation or with the surface adsorption/desorption of protons/alkali cations inside the tunnels of α-MnO_2 crystal (Scheme 2).[53] In case of thin film electrodes, the oxidation state of Mn changes between III and IV during the charge-discharge process.[53] However, in case of thicker composite electrodes, only the surface layer of the electrode involves in the charge storage process and no change in the oxidation state was noticed.[53] In our case, the charge storage mechanism is believed to involve the surface adsorption/desorption of electrolyte cations due to the mesoporous nature of α-MnO_2. The cyclic voltammetric response at slow scan rate of 2 mV/sec shows a broad ill-defined anodic and cathodic wave in the potential range of 450-600 mV (ESI 6), suggesting the possible intercalation-de-intercalation of metal cations during the electrode reaction. The specific capacitance was measured from the charge-discharge curves (Figure 6b) and was 322 F g^{-1}. To further evaluate the performance of the material, the electrochemical impedance measurements were performed at the potential of 0.5 V (Ag/AgCl). Interestingly, in the high frequency region, a near vertical Warburg line with a rapid increase in Z_{im} along the Y axis was observed. Such impedance features indicate the ideal capacitive behaviour of the electrode and the free diffusion of ions through the porous structure of α-MnO_2. The charge transfer resistance was calculated to be 7.6 Ω (ESI 7). The rate capability was evaluated by measuring the capacitance at different current density. The electrode retains >80% of its initial capacitance obtained at 1 A g^{-1} even at 20 A g^{-1} (ESI 8). The excellent rate capability is due to the decrease in the dynamic resistance of the electrolyte ions within the 3D mesoporous structure, which provide channels for the free

transportation of electrolyte ions.[54] The cycling stability was tested by 8,000 repeated charge-discharge cycles at high current density of 20 A g^{-1} (Figure 6d). Interestingly, our mesoporous α-MnO_2 could retain 90% of the initial specific capacitance even after 8,000 repeated cycles. The α-MnO_2 electrode retains 100% of its initial capacitance even after 3000 continuous charge-discharge cycles due to the presence of mesoporous 3-dimensional network structure, highlighting the remarkable recyclability of the material. Moreover, it retains >95% efficiency during the extensive cycles. It is worth pointing out here that the amount of Zn/Zn(II) present in the sample influences the specific capacitance of α-MnO_2. For instance, enhancement in the specific capacitance was noticed while increasing the Zn content from 0.45 to 0.98 atomic %. Further increase in the Zn content does not improve the capacitive performance (Table S2). The mesoporous nature, large surface area and high electronic conductivity of α-MnO_2 contribute to the enhancement in the overall performance.

To understand the effect of extensive charge-discharge cycles on the surface structure and morphology, if any, of the electrode material, post-mortem analysis was performed with TEM and XRD measurements after 3000 cycles at the current density of 20 A/g. The post mortem TEM analysis of the α-MnO_2 electrode after 3000 charge-discharge cycles shows the partial disintegration of the initial hierarchical 3D flower-like structure (Figure 7 a, b). The careful analysis of the HRTEM image (Figure 7 c) shows that the MnO_2 retains its original α phase; lattice fringe spacing of 4.9 and 3.01 Å, corresponding to the (200) and (301) plane of α-MnO_2 was observed (Figure 7 c). This was further confirmed with the XRD analysis; all the diffraction patterns are assigned to α-MnO_2 (Figure 7d). Although partial disintegration of 3-D hierarchical structure and observable decrease in the particle size was observed after the charge-discharge cycles, the MnO_2 retains its original α phase. The change in the % retention of specific capacitance after 3000 cycles (Figure 6 a, b) could be due to the partial disintegration of the α-MnO_2 structure. It is interesting to note that the MnO_2 nanostructure

has the hierarchical structure even after extensive cycles, though it is partially disintegrated.

To further evaluate the capacitive performance of the material, ASC was made by pairing α-MnO_2 with rGO anode using a stainless steel split flat cell. rGO was prepared from GO according to the procedure reported elsewhere[55] and characterized by FTIR, XRD and XPS analysis (ESI 9). rGO was rationally selected to pair with α-MnO_2 as it has wide potential window, high electronic conductivity and mechanical strength. As the α-MnO_2 sample containing 0.98% of Zn exhibits high specific capacitance, it was used in the fabrication of ASC. Rectangular shaped voltammetric response with a wide potential window of 0 to 2 V was obtained (Figure 8). It is interesting to note that we could achieve a potential window of 2 V in aqueous solution with α-MnO_2 and rGO based ASC. Our MnO_2-based electrode could be polarized up to 1.2 V (NHE) in neutral pH due to high oxygen overpotential. Similarly our rGO-based electrode could be polarized up to -0.8 V (NHE) due to hydrogen overpotential (ESI 10). Consequently we could achieve a practical cell voltage of 2 V in aqueous solution. This is in accordance with the earlier literature.[56] The specific capacitance was calculated from the charge-discharge curves and the device shows a specific capacitance of 63.5 F g^{-1} at the current density of 2 A g^{-1}. The energy density of device was calculated to be 35.28 Wh kg^{-1} at the power density of 2.0 kW kg^{-1} and could also retain 27.78 Wh kg^{-1} at a power density of 16.67 kW kg^{-1}. The energy and power density of our device is higher than that of the existing MnO_2-based ASC[57,58] (Table S3). It is worth pointing out here that the device could retain 100% of its initial specific capacitance even after 3000 repeated charge-discharge cycles at high current density of 10 A g^{-1}, highlighting its excellent cycling stability (Figure 8c, ESI 11). The superior performance of ASC can be ascribed to the enhanced accessibility of the material to the electrolyte due to the mesoporous 3D structure.

It is worth comparing the electrochemical performance of our hierarchical α-MnO_2 with the existing porous/mesoporous MnO_2-based electrodes in terms of specific capacitance, energy

density, rate capability, cycling stability, etc. (Table S3 and S4). The existing MnO_2-based electrodes show specific capacitance ranging from 180 to 460 F g^{-1}, depending on the current density (0.1-6 A g^{-1}) or scan rate (1-5 mV s^{-1}) in aqueous neutral solution.[36,59-60] The rate capability of most of the MnO_2-based electrodes is rather poor; >40% decrease in the initial capacitance was noticed at the current density 10-20 A g^{-1}.[36,59-62] The cycling stability is one of the main parameters that decide the practical utility of the material for device fabrication. Significant loss of the initial specific capacitance after extensive charge-discharge cycles has been observed. For instance, 20-30% decrease in the initial specific capacitance after 3000 cycles at the current density of 5-10 A g^{-1} has been observed.[59,62,63] Wu and co-workers achieved superior cycling stability (>94% after 10000 to 23000 cycles) with Na_xMnO_2, K_xMnO_2 and MnO_2 nanorod-based ASC, though the energy density is rather low (17 Wh kg^{-1} at 2 kW kg^{-1}).[57,58,64-65] In our case, we have achieved an energy density of 35.28 Wh kg^{-1} at 2 kW kg^{-1} with the ASC. Our electrode could retain 80% of the initial capacitance even at 20 A g^{-1} and it has very good cycling stability; more than 90% of the capacitance was retained after 8000 extensive charge-discharge cycles at high current density of 20 A g^{-1} in three- electrode configuration. Our ASC retains 100% of the initial capacitance after 3000 charge-discharge cycles. The superior performance can be ascribed to the 3D hierarchical structure of the materials.

The examination of self-discharge characteristics of the supercapacitor is important to evaluate the performance of ASC for practical applications. The self-discharge of the device is largely depends on the nature of the electrode materials, purity of the electrolyte, etc. The loss of charge can be due to the diffusion of charge and restructuring of electrolyte ions inside the electrode material. It is generally accepted that the self-discharge mechanism can be of faradaic or ohmic.[2,66] In the faradaic type mechanism, the charge redistribution and presence of impurities actually cause the loss of charge. We have evaluated the self-discharge

characteristics of ASC prepared with the three different α-MnO_2 samples containing varying amount of Zn (ESI 12). As our study is of fundamental interest, the discharge profile was acquired only for period of 15,000 s. It was found that the device made with α-MnO_2 sample containing large amount of Zn undergoes fast discharge whereas slow discharge was noticed for the samples containing less amount of Zn. The plot of *V* against square root of *t* is near linear, suggesting that the mechanism of discharge could be due to the presence of Zn impurity.[2,66]

Conclusion

Facile reduction of Mn(VII) using metallic Zn and the growth of nanocrystalline mesoporous α-MnO_2 of 3D flower-like structure with large surface area for the development of high energy density aqueous asymetric supercapacitor are demonstrated. Our synthetic method is rapid and the mesoporous structure was achieved at room teperature without any templates. Reduction of MnO_4^- was achieved by its thermodynamically favourable reaction with Zn and the in situ generated nascent hydrogen. The electronic conductivity of α-MnO_2 is higher than the traditional commercial MnO_2. The porous morphology and the large surface area of α-MnO_2 favor the easy transportation of electrolyte ions and exhibit excellent supercapacitive performance. The high specific capacitance, remarkable recyclability and rate capability of our mesoporous α-MnO_2 outperforms the conventional α-MnO_2 nanoparticles. High energy density ASC was fabricated by pairing the mesoporous α-MnO_2 with rGO anode and it shows excellent cycling stability with 100 % retention of the capacitance even after 3000 repeated charge-discharge cycles.

Acknowledgements

We acknowledge Dr. Sumanta Kumar Sahu and Angshuman Ray Chowdhuri, ISM Dhanbad for BET measurement. We are also thankful to Dr. Achintya Singha, Bose Institute,

Kolkata for Raman measurement and department of Physics, Indian Institute of Technology Kharagpur for XPS measurements. We thank Prof. Chacko Jacob, Materials Science Center, IIT Kharagpur for fruitful discussion. This work was financially supported by Department of Science and Technology and Council of Scientific and Industrial Research, New Delhi. SB is a recipie nt of UGC research fellowship.

Electronic supplimentry information:

HRTEM images, Raman spectral and EDS profiles of MnO_2, equivalent circuit, plot illustrating the rate capability, repeated charge-discharge curve of ASC and table summarizing the electrical conductivity of MnO_2, existing method for the synthesis of porous MnO_2, and the perforomance of existing MnO_2-based electrodes and ASCs.

AUTHOR INFORMATION

Corresponding Author

*Tel.: +91 3222 283348. E-mail: crraj@chem.iitkgp.ernet.in

References

1. F. Béguin and E. Frąckowiak (Eds), *Supercapacitors: Materials, Systems, and Applications*, Wiley-VCH, Weinheim, Germany, 2013.
2. B. E. Conway, *Electrochemical Supercapacitors: Scientific Fundamentals and Technological Applications*, Kluwer Academic/Plenum Publisher, New York, 1999.
3. P. Thounthong, B. Raël and B. Davat, *J. Power Sources*, 2009, **193**, 376–385.
4. M. Winter and R. J. Brodd, *Chem. Rev*., 2004, **104**, 4245-4269.
5. H. Jiang, C. Li, T. Sun and J. Ma, *Nanoscale*, 2012, **4,** 807-812.
6. Y. Yan, Q. Cheng, G. Wang and C. Li, *J. Power Sources*, 2011, **196**, 7835– 7840.
7. Y. Yan, Q. Cheng, Z. Zhu, V. Pavlinek, P. Saha and C. Li, *J. Power Sources*, 2013, **240**, 544-550.
8. Z. Zhu, Y. Hu, H. Jiang and C. Li, *J. Power Sources*, 2014, **246**, 402-408.
9. H. Jiang, P. S. Lee and C. Li, *Energy Environ. Sci*., 2013, **6**, 41-53.
10. H. Jiang, J. Ma and C. Li, *Adv. Mater*., 2012, **24**, 4197–4202.
11. M. Sevilla and R. Mokaya, *Energy Environ. Sci*., 2014, **7**, 1250-1280.
12. S. Bag and C. R. Raj, *J. Mater. Chem. A*, 2014, **2**, 17848-17856.
13. G. Wang, L. Zhang and J. Zhang, *Chem. Soc. Rev*., 2012, **41,** 797-828.
14. X. Lang, A. Hirata, T. Fujita and M. Chen, *Nature Nanotech*., 2011, **6**, 232–236.
15. V. Subramanian, H. Zhu, R. Vajtai, P. M. Ajayan and B. Wei, *J. Phys. Chem. B*, 2005, **109**, 20207-20214.
16. J. Yan, A. Sumboja, X. Wang, C. Fu, V. Kumar and P. S. Lee, *Small*, 2014, **10**, 3568–3578.
17. Y. Zhao, W. Ran, J. He, Y. Huang, Z. Liu, W. Liu, Y. Tang, L. Zhang, D. Gao and F. Gao, *Small*, 2015, **11**, 1310-1319.
18. X. Sun, Q. Li, Y. Lu and Y. Mao, *Chem. Commun*., 2013, **49**, 4456-4458.

19. R. S. Kalubarme, H. S. Jadhav and C. J. Park, *Electrochim. Acta*, 2013, **87**, 457-465.

20. J. Jiang and A. Kucernak, *Electrochim. Acta*, 2002, **47**, 2381-2386.

21. J. B. Fei, Y. Cui, X. H. Yan, W. Qi, Y. Yang, K. W. Wang, Q. He and J. B. Li, *Adv. Mater*., 2008, **20**, 452–456.

22. J. Ge, H.-B. Yao, W. Hu, X.-F. Yu, Y.-X. Yan, L.-B. Mao, H.-H. Li, S.-S. Li and S.-H. Yu, *Nano Energy*, 2013, **2**, 505–513.

23. X. Wang and Y. Li, *Chem. Commun*., 2002, 764-765.

24. X. Xie, C. Zhang, M.-B. Wu, Y. Tao, W. Lv and Q.-H. Yang, *Chem. Commun*., 2013, **49**, 11092-11094.

25. S. L. Chou, J. Z. Wang, S. Y. Chew, H. K. Liu and S. X. Dou, *Electrochem.Commun*., 2008, **10**, 1724−1727.

26. L. Li, Z. A. Hu, N. An, Y. Y. Yang, Z. M. Li and H. Y. Wu, *J. Phys. Chem. C*., 2014, **118**, 22865-22872.

27. S. W. Lee, J. Kim, S. Chen, P. T. Hammond and S. Yang, *ACS Nano*, 2010, **4**, 3889-3896.

28. X. F. Xie and L. Gao, *Carbon*, 2007, **45**, 2365−2373.

29. Y. Li, G. Wang, K. Ye, K. Cheng, Y. Pan, P. Yan, J. Yin and D. Cao, *J. Power Sources*, 2014, **271**, 582-588.

30. H. Cheng, L. Long, D. Shu, J. Wu, Y. Gong, C. He, Z. Kang and X. Zou, *Int. J. Hydrogen Energy*, 2014, **39**, 16151-16161.

31. C.-C. Wang, H.-C. Chen and S.-Y. Lu, *Chem. Euro. J*., 2014, **20**, 517-523.

32. S. X. Deng, D. Sun, C. H. Wu, H. Wang, J. B. Liu, Y. X. Sun and H. Yan, *Electrochim. Acta*, 2013, **111**, 707-712.

33. P. Yu, X. Zhang, D. Wang, L. Wang and Y. Ma, *Cryst. Growth Des*., 2009, **9**, 528-533.

34. Y. Liu, Z. Chen, C. H. Shek, C. M. L. Wu and J. K. L. Lai, *ACS Appl. Mater. Interfaces*, 2014, **6**, 9776-9784.

35. X. Duan, J. Yang, H. Gao, J. Ma, L. Jiao and W. Zheng, *Cryst. Eng. Comm*., 2012, **14,** 4196-4204.

36. J. J. Zhu, L. L. Yu and J. T. Zhao, *J. Power Sources*, 2014, **270**, 411-417.

37. Y. T. Wang, A. H. Lu, H. L. Zhang and W. C. Li, *J. Phys. Chem. C*, 2011, **115**, 5413–5421.

38. W. S. Hummers and R. E. Offeman, *J. Am. Chem. Soc*., 1958, **80**, 1339-1339.

39. K. Chen, D. Xue and S. Komarneni, *J. Power Sources*, 2015, **279**, 365-371.

40. S. He, H. Hou and W. Chen, *J. Power Sources*, 2015, **280**, 678-686.

41. V. Ganesh, S. Pitchumani and V. Lakshminarayanan, *J. Power Sources*, 2006, **158**, 1523–1532.

42. B. Li, G. Rong, Y. Xie, L. Huang and C. Feng, *Inorg. Chem*., 2006, **45**, 6404-6410.

43. S. Bag, K. Roy, C. S. Gopinath and C. R. Raj, *ACS Appl. Mater. Interfaces*, 2014, **6**, 2692-2699.

44. J. Luo, H. T. Zhu, H. M. Fan, J. K. Liang, H. L. Shi, G. H. Rao, J. B. Li, Z. M. Du and Z. X. Shen, *J. Phys. Chem. C*, 2008, **112**, 12594-12598.

45. R. Chen, J. Yu and W. Xiao, *J. Mater. Chem. A*, 2013, **1**, 11682-11690.

46. C. Wei, L. Yu, C. Cui, J. Lin, C. Wei, N. Mathews, F. Huo, T. Sritharan and Z. Xu, *Chem. Commun*., 2014, **50**, 7885-7888.

47. Q. Li, Z. L. Wang, G. R. Li, R. Guo, L. X. Ding and Y. X. Tong, *Nano Lett*., 2012, **12**, 3803−3807.

48. S. Devaraj and N. Munichandraiah, *J. Phys. Chem. C*, 2008, **112**, 4406-4417.

49. W. Wei, X. Cui, W. Chen and D. G. Ivey, *Chem. Soc. Rev*., 2011, **40**, 1697–1721.

50. C. Xu, H. Du, B. Li, F. Kang and Y. Zeng, *Electrochem. Solid-State Lett.*, 2009, **12**,

A61-A65.

51. C. Xu, B. Li, H. Du and F. Kang, *Angew. Chem. Int. Ed.*, 2012, **51**, 933 –935.
52. B. Lee, H. R. Lee, H. Kim, K. Y. Chung, B. W. Cho and S. H. Oh, *Chem. Commun*., 2015, **51**, 9265-9268.
53. M. Toupin, T. Brousse and D. Bélanger, *Chem. Mater*., 2004, **16**, 3184-3190.
54. L. Zhang and G. Shi, *J. Phys. Chem. C,* 2011, **115**, 17206–17212.
55. S. Bag, B. Mondal, A. K. Das and C. R. Raj, *Electrochim. Acta*, 2015, **163**, 16-23.
56. V. Khomenko, E. Raymundo-Piñero and F. Béguin, *J. Power Sources*, 2006, **153**, 183–190.
57. Q. T. Qu, Y. Shi, S. Tian, Y. H. Chen, Y. P. Wu and R. Holze, *J. Power Sources*, 2009, **194**, 1222–1225.
58. Q. T. Qu, L. Li, S. Tian, W. Guo, Y. Wu and R. Holze, *J. Power Sources*, 2010, **195**, 2789–2794.
59. L. Zhao, J. Yu, W. Li, S. Wang, C. Dai, J. Wu, X. Bai and C. Zhi, *Nano Energy*, 2014, **4**, 39–48.
60. J. Zhu, W. Shi, N. Xiao, X. Rui, H. Tan, X. Lu, H. H. Hng, J. Ma and Q. Yan, *ACS Appl. Mater. Interfaces*, 2012, **4**, 2769−2774.
61. M. Huang, Y. Zhang, F. Li, L. Zhang, R. S. Ruoff, Z. Wen and Q. Liu, *Sci. Rep.*, 2014, **4**, 3878-3885.
62. M. Kundu and L. Liu, *J. Power Sources*, 2013, **243**, 676-681.
63. J. Zhu, S. Tang, H. Xie, Y. Dai and X. Meng, *ACS Appl. Mater. Interfaces*, 2014, **6**, 17637–17646
64. Q. T. Qu, P. Zhang, B. Wang, Y. Chen, S. Tian, Y. Wu and R. Holze, *J. Phys. Chem. C* 2009, **113**, 14020–1402.
65. F. Wang, S. Xiao, Y. Hou, C. Hu, L. Liu and Y. Wu, *RSC Adv.*, 2013, **3**, 13059–13084.

66. A. Yu, V. Chabot, J. Zhang, Electrochemical supercapacitors for energy storage and delivery: Fundamentals and applications, CRC Press, Taylor and Francis Group, Boca Raton, FL, 2013.

Figures and Scheme

Scheme 1

Zn-mediated reduction of $KMnO_4$ and growth of mesoporous MnO_2.

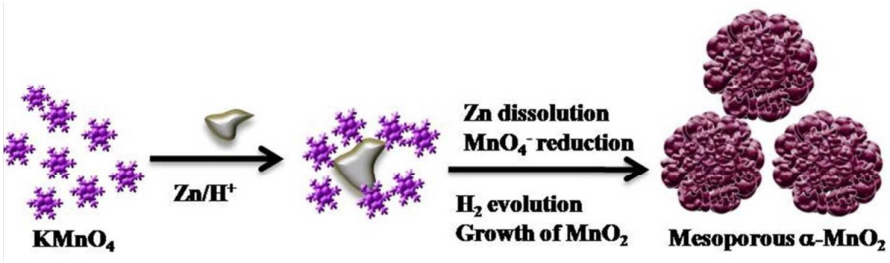

Scheme 2

The structure of α-MnO_2.

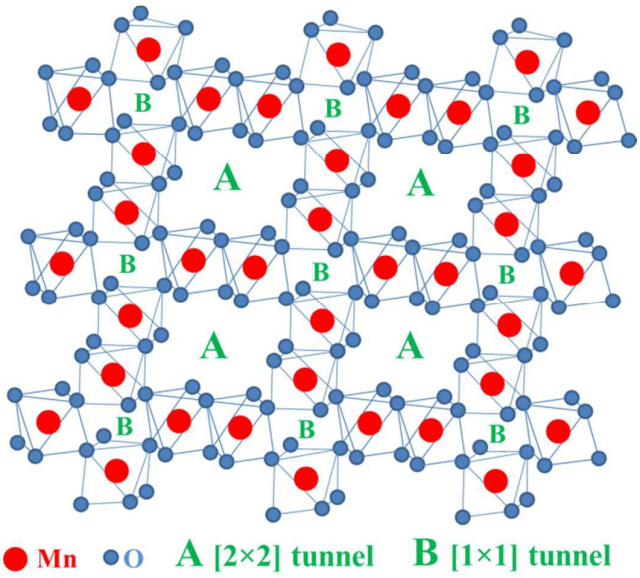

Figure 1

TEM (a-c), HRTEM (d) and FESEM (e, f) images of as-grown α-MnO_2. Red squares in the TEM images indicate the magnified parts.

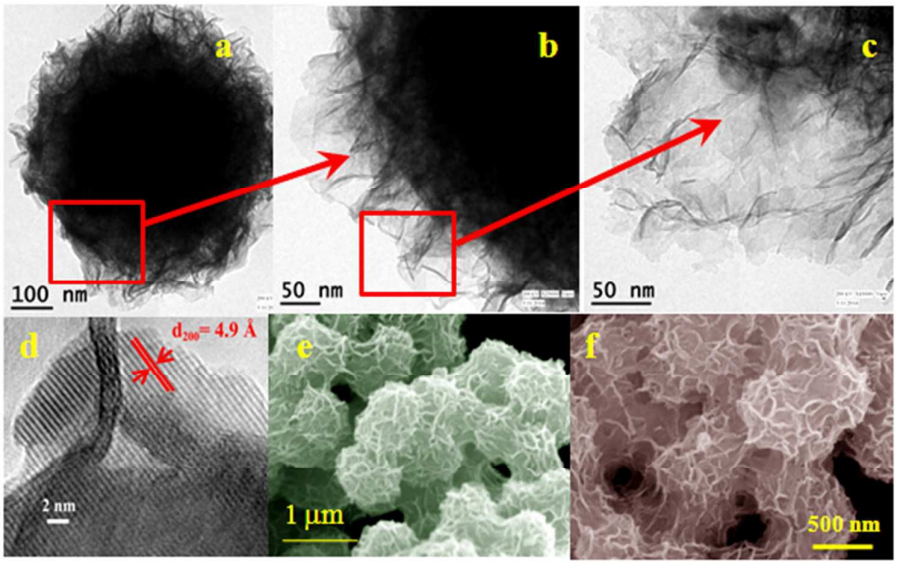

Figure 2

TEM images obtained at different time interval during growth of α- MnO_2 nanostructure. (a-c): 15 and (d-f) 60 min of the reaction.

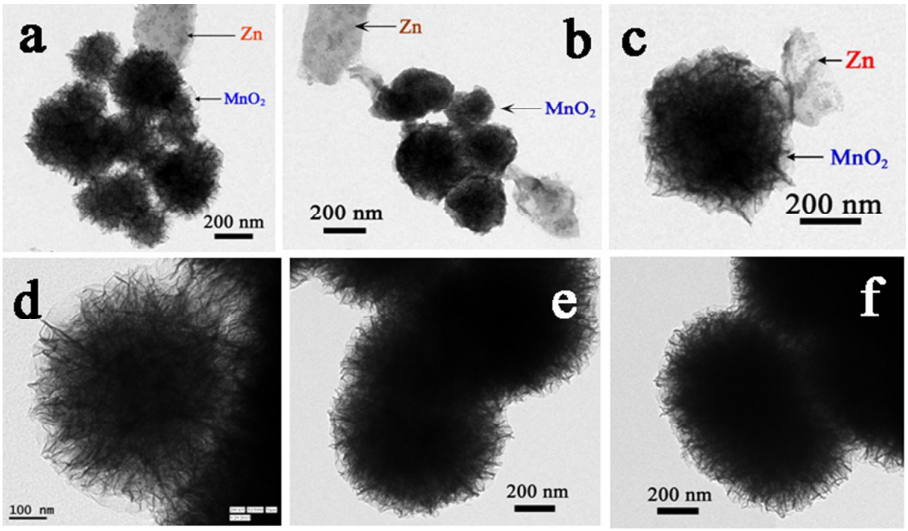

Figure 3

XRD profile of as-grown α-MnO_2

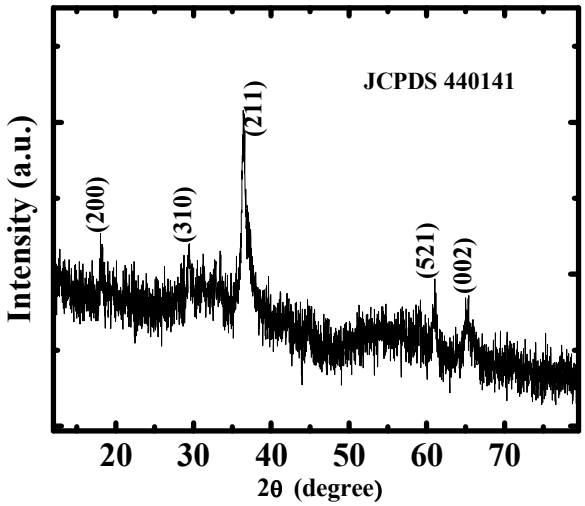

Figure 4

Survey scan (a) and high resolution Mn 2p (b) and Mn 3s (c) XPS profiles of as-grown α-MnO_2. The high resolution XPS profile of trace amount of Zn is shown in (d).

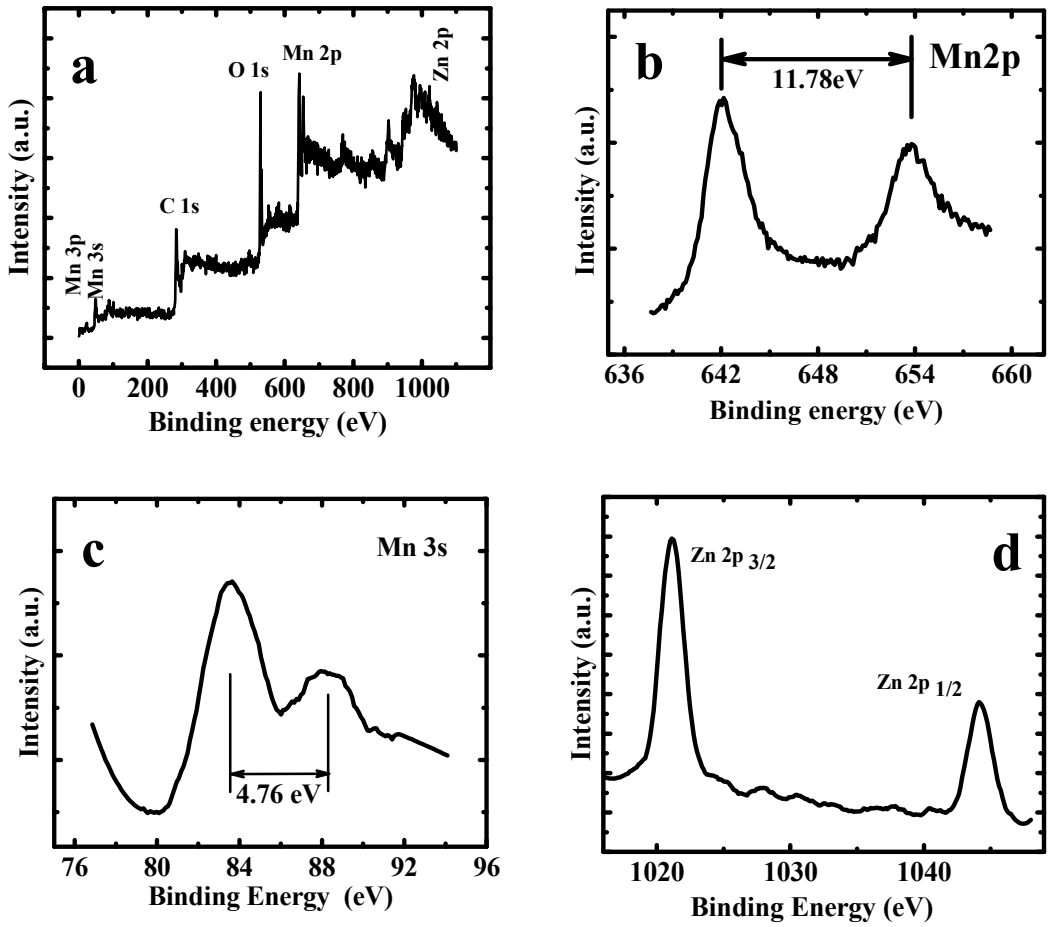

Figure 5

BET adsorption-desorption (a) and Barrett−Joyner−Halenda pore size analysis (b) profiles of α-MnO_2.

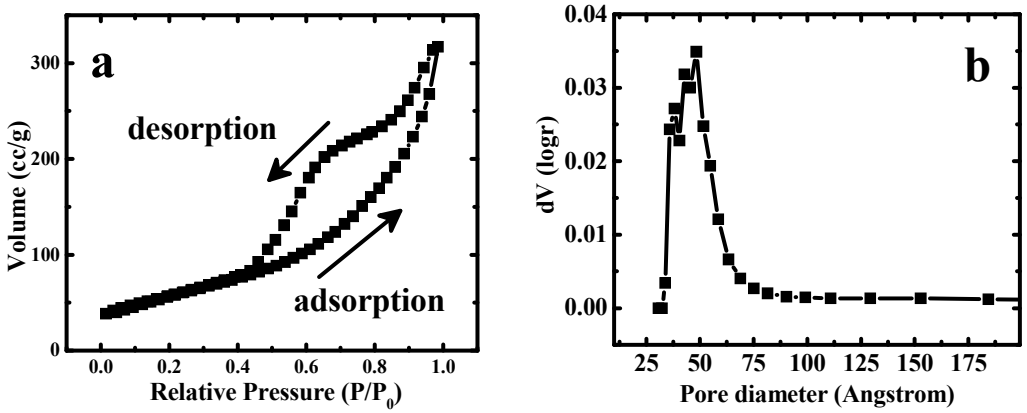

Figure 6

Cyclic voltammetric (a), galvanostatic charge-discharge (b) and impedance profiles (c) of MnO_2 in 1 M Na_2SO_4. Inset in (c) is the magnified region of the Nyquist plot. Plot illustrating the specific capacitance and columbic efficiency retention during 8000 charge-discharge cycles is shown in (d).

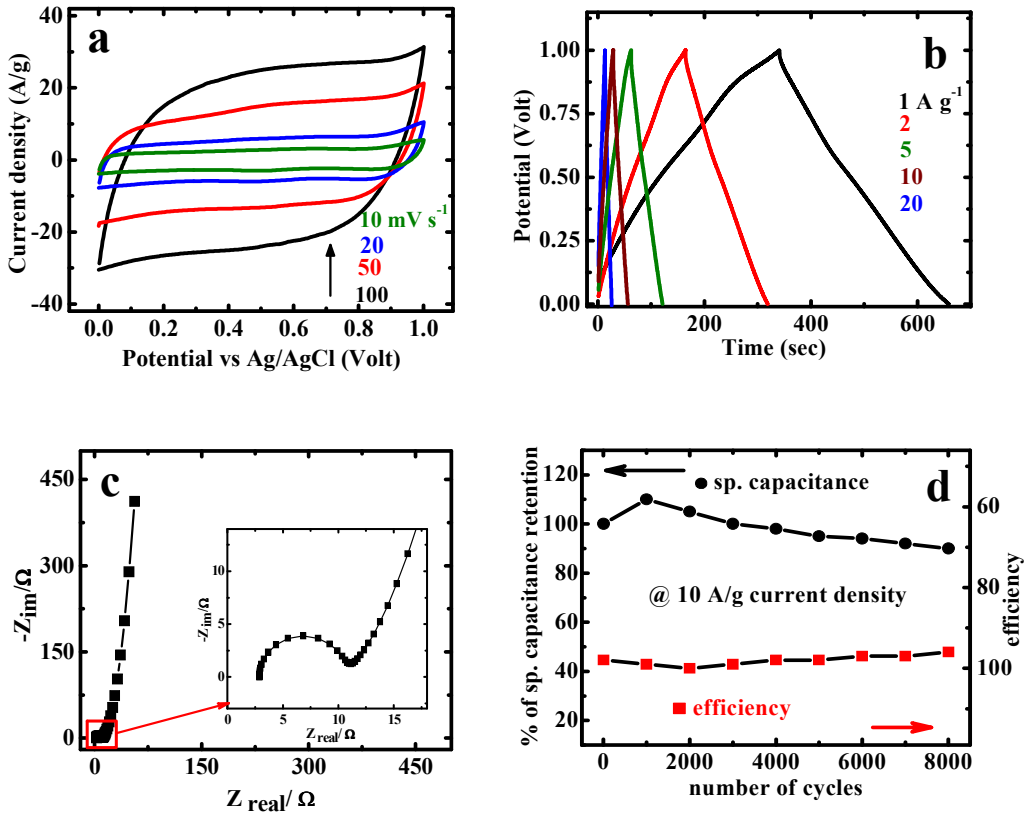

Figure 7

Post-mortem TEM (a,b), HRTEM (c) and XRD analysis (d) of the α-MnO_2 electrode. The samples were subjected to TEM and XRD analysis after 3000 charge-discharge cycles at the current density of 20 A g^{-1}.

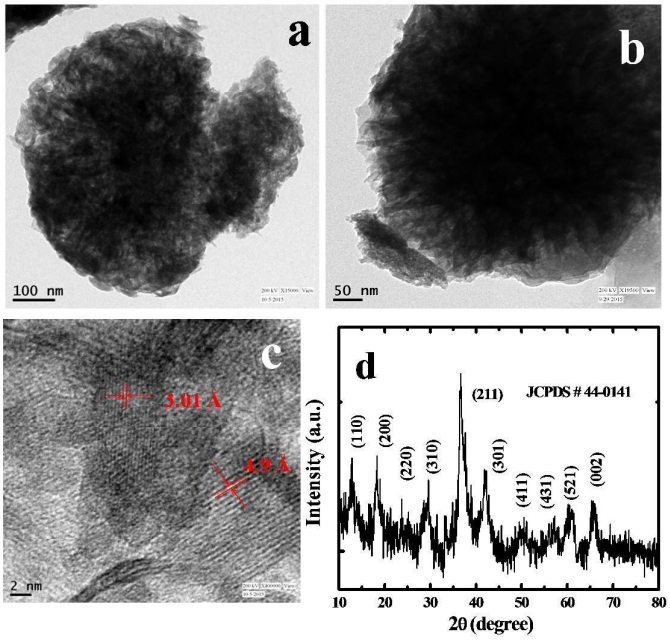

Figure 8

(a) Cyclic voltammogram at different scan rate and (b) charge-discharge curves at various current densities illustrating the performance of ASC in 1 M Na_2SO_4. (c) Plot illustrating the retention of specific capacitance during repeated charge-discharge cycles. (d) Electrochemical impedance response of the ASC. Inset shows the magnified part of the high frequency region.

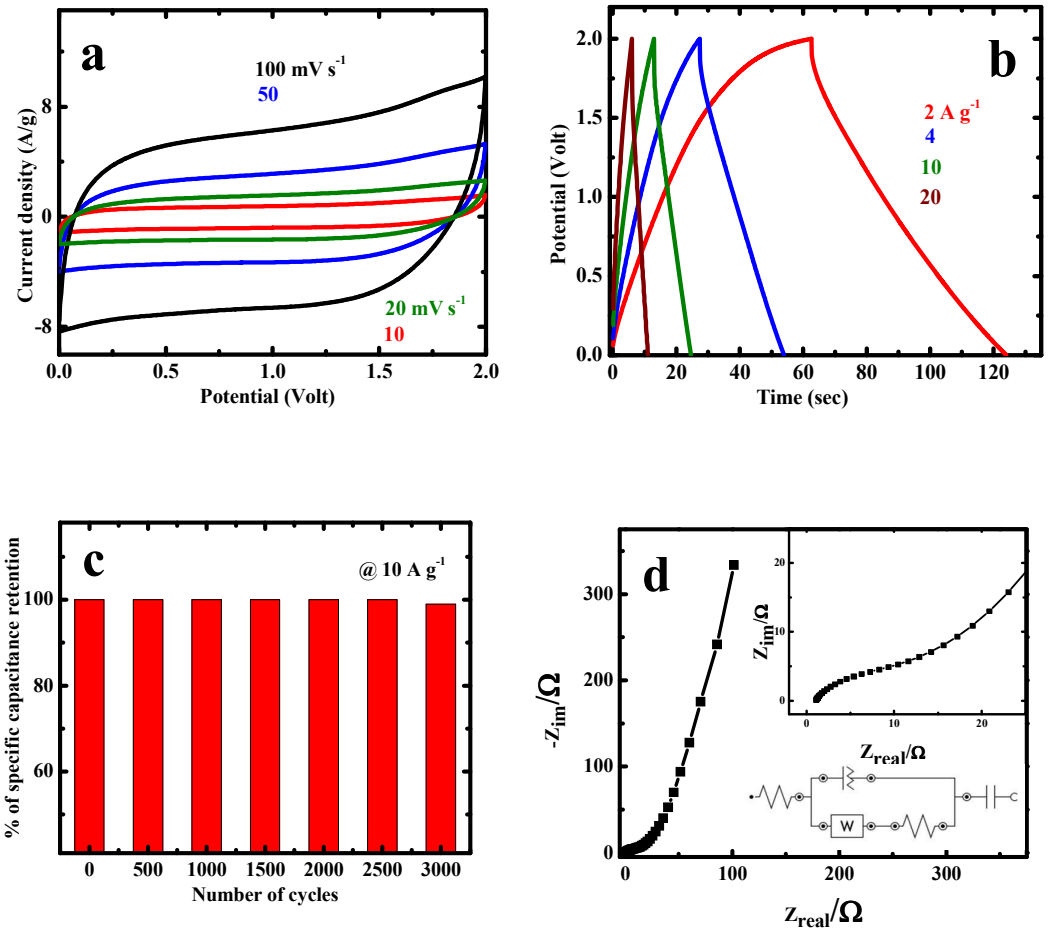

Graphical abstract

Hierarchical Three-Dimensional Mesoporous MnO_2 Nanostructure for High Performance Aqueous Asymmetric Supercapacitor

Sourav Bag and C. Retna Raj*

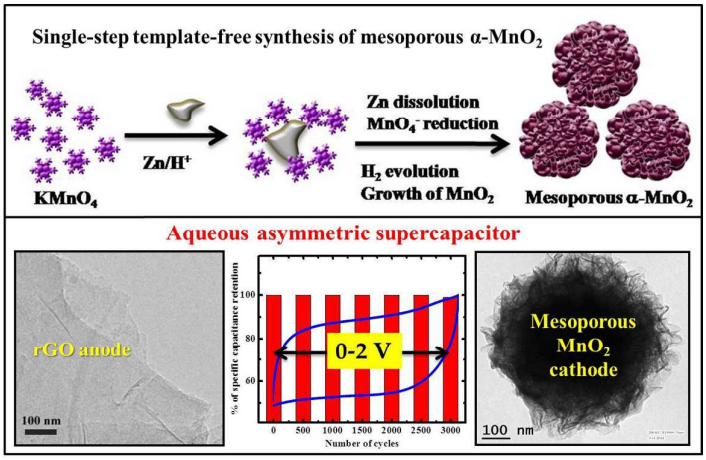

Highlight: Nanocrystalline mesoporous α-MnO_2 is synthesized for the fabrication of high energy density aqueous asymmetric supercapacitor device.